Journal of Hazardous Materials 401 (2021) 123355

Contents lists available at ScienceDirect

Journal of Hazardous Materials

journal homepage: www.elsevier.com/locate/jhazmat

In-situ self-assembly construction of hollow tubular g-C_3N_4 isotype heterojunction for enhanced visible-light photocatalysis: Experiments and theories

Qinghua Liang[a,1], Xiaojuan Liu[b,1], Jiajia Wang[a,1], Yang Liu[a,1], Zhifeng Liu[a,*], Lin Tang[a,*], Binbin Shao[a], Wei Zhang[b], Shanxi Gong[c], Min Cheng[a], Qingyun He[a], Chengyang Feng[a]

[a] College of Environmental Science and Engineering, Hunan University and Key Laboratory of Environmental Biology and Pollution Control (Hunan University), Ministry of Education, Changsha, 410082, PR China
[b] The First Affiliated Hospital of Hunan University of Chinese Medicine, Changsha, 410007, PR China
[c] School of Chemistry and Chemical Engineering, Guangxi University, Nanning 530004, PR China

GRAPHICAL ABSTRACT

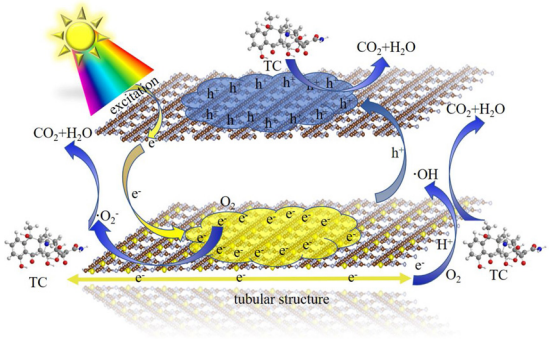

ARTICLE INFO

Editor: Xiaohong Guan

Keywords:
g-C_3N_4 isotype heterojunction
Self-assembly
Visible-light photocatalysis
Theoretical calculation
Degradation pathway

ABSTRACT

A highly reactive hollow tubular g-C_3N_4 isotype heterojunction (SCN-CN) was designed to enhance visible light absorption and manipulate the directed transfer of electrons and holes. The results of UV–vis DRS, XPS valence band and DFT theoretical calculations indicated S doping increases the visible-light absorption capacity and changed the ba nd gap structure of g-C_3N_4 (CN), resulting in the transfer of electrons from the CN to the SCN and holes from the SCN to the CN under visible light. In addition, the tubular structure of the SCN-CN facilitated the transfer of electrons in the longitudinal direction, which reduced charge carrier recombination. Furthermore, the optical properties, electronic structure, and electron transfer of SCN-CN were also studied by experiments and theoretical calculations. The antibiotic tetracycline hydrochloride (TCH) and dye Rhodamine B (RHB) were subjected to evaluate the photocatalytic performance of SCN-CN. The scavenger tests and ESR data showed that the h^+, $·O_2^-$ and ·OH worked together in the photocatalytic process. Moreover, the photocatalytic degradation pathway was analyzed by LC-MS. This study synthesized a hollow tubular CN isotype heterojunction with high visible-light photocatalytic performance and provided a theoretical basis for CN isotype heterojunction.

* Corresponding authors.
E-mail addresses: zhifengliu@hnu.edu.cn (Z. Liu), tanglin@hnu.edu.cn (L. Tang).
[1] The authors contribute equally to this paper.

https://doi.org/10.1016/j.jhazmat.2020.123355
Received 27 April 2020; Received in revised form 9 June 2020; Accepted 25 June 2020
Available online 03 July 2020

1. Introduction

In recent years, energy shortages and environmental pollution have become the focus of attention in the world (Liu et al., 2019a; Jiang et al., 2018a; Shao et al., 2019a; Liu et al., 2012; He et al., 2019). Photocatalysis is an effective means to solve these problems by using solar energy, which being studied for hydrogen production, CO_2 reduction, ammonia synthesis and degradation of pollutants, due to its environmental friendliness, low cost and good reusability (Liang et al., 2019; Shao et al., 2019b; Wu et al., 2020; Pan et al., 2020; Romanos et al., 2020). How to obtain a photocatalyst with good photocatalytic properties is crucial, and researchers are committed to this. In general, the photocatalytic performance mainly depends on the band gap structure of the semiconductor (band gap, valence band, conduction band and Fermi level position), specific surface area, pore structure, apparent morphology light absorption capacity, and charge carrier recombination rate (Feng et al., 2018; Yu et al., 2019; Liu et al., 2019b; Triantis et al., 2020).

Recently, non-metallic polymer g-C_3N_4 (CN) has received great attention in photocatalytic degradation of contaminant systems due to its suitable band gap (2.7 eV) (Chen et al., 2019; Luo et al., 2019; Li et al., 2016). CN can be obtained by simple thermal polymerization through precursors, such as melamine and urea. However, CN has low photocatalytic efficiency, due to its low visible light (VSL) absorption capacity, rapid charge carrier recombination, and small specific surface area (Shao et al., 2019c; Wang et al., 2017). In order to improve its photocatalytic performance under visible light, researchers have done a lot of research work, such as doping metal/non-metal, constructing composites (Tang et al., 2018), introducing vacancy defects (Liu et al., 2019c; Sun et al., 2019a) and changing the morphology (Guo et al., 2016), where the isotype heterojunction is a good choice to improve photocatalyst performance without relying on other semiconductors (Yang et al., 2016; Li et al., 2017). An isotype heterojunction is created by changing the band gap structure of the original semiconductor, and then it is combined with the original semiconductor to construct an isotype heterojunction (Wang et al., 2019a; Zhang et al., 2012). Due to this unique electronic band structure, both semiconductors can generate electrons and holes through light. Meanwhile, the electrons and holes are transferred at the heterojunction interface, which can reduce the recombination of photoinduced e^--h^+ pairs and improve the photocatalytic efficiency.

As of now, only a few studies on CN isotype heterojunctions have been reported, which mainly divided into different carbon nitride raw materials (urea, melamine) (Dong et al., 2013; Liu et al., 2017; Liang et al., 2017), different dimensions (0D, 1D, 2D) (Wang et al., 2019b; Mahzoon et al., 2018), and element doping (B, S, P, Cl) (Yang et al., 2016; Ruan et al., 2017; Jiang et al., 2018b). In particular, Tong et al. first self-assembled melamine and cyanuric acid, and then combined with urea to obtain 1D tubular CN isotype heterojunction (Tong et al., 2016). Tong's study showed that the 1D tubular CN isotype heterojunction had efficient photocatalytic hydrogen production efficiency owing the tubular structure capable of manipulating the directional collection and transfer of electrons. However, the morphology of the tubular CN isotype heterojunction of Tong's obtained is poor and the visible light absorption ability is weak.

Meanwhile, theoretical calculations have important value in analyzing the electronic structural properties, optical properties, work functions and charge transfer, and degradation mechanisms of photocatalysts (Liu et al., 2018a; Zhao et al., 2019; Liu et al., 2018b, c; Shao et al., 2020). Theoretical calculations are also widely used in the development and design of new photocatalysts, the types and positions of doped elements, the charge transfer at the interface of composite heterojunctions, as well as the thermodynamics and kinetics of chemical reactions (Zhu et al., 2017; Sun et al., 2019b; Liu et al., 2016). The combination of theoretical calculations and experiments, which complement each other, has become the current trend. Zheng et al. used a combination of experiments and theory to study the mechanism of degradation of bisphenol A by dual-oxygen-doped porous g-C_3N_4 (Zhang et al., 2019a). Through theoretical calculations, the band gap, the density of states and the differential density of charges of the oxygen-doped porous g-C_3N_4 were studied. In addition, the theoretical calculation of the degradation mechanism and the intermediate product were used to search the transition state.

Consequently, it is worthwhile to study how to obtain a hollow tubular CN with good morphology and strong VSL absorption capacity. Moreover, based on the fact that the theoretical basis of CN isotype heterojunction is lacking, it is important to reveal the structural properties, electron transfer and degradation mechanism of tubular CN isotype heterojunction photocatalysts by a combination of theoretical calculations and experiments.

In this study, the hollow tubular S-doped CN isotype heterojunction (SCN-CN) with good morphology and strong VSL absorption capacity was firstly prepared by in situ self-assembled melamine, trithiocyanuric acid and urea. The SCN-CN exhibited significantly improved visible light removal of TCH and RHB, which was attributed to the construction of heterojunctions, S-doping and hollow tubular structures. This unique composite structure led to its strong visible light absorption ability and good charge separation ability. This work proved that the hollow tubular g-C_3N_4 isotype heterojunction constructed by simple in-situ self-assembly technology had strong visible light photocatalytic performance, and it had good application potential in the environmental field.

2. Experimental

2.1. Chemicals and materials

Melamine was obtained from Sinopharm Chemical Reagent Co., Ltd (Shanghai, China). Trithiocyanuric acid was obtained from 9 din. Biotechnology Co., Ltd (Shanghai, China). TCH was purchased from Bomei biological technology Co., Ltd (Hefei, China). The RHB was provided by Tianjin Fuyu Fine Chemical Co. Ltd (Tianjin, China). The ultrapure water (18.25 MΩ cm^{-1}) was used throughout the experiment.

2.2. Construction of SCN-CN isotype heterojunction

For tubular SCN-CN composite material, the band gap structure of S-doped carbon nitride (SCN) was adjusted by doping different amounts of S atoms in CN. Then, the SCN with a suitable band gap structure was combined with CN to construct the SCN-CN composite material. The SCN-CN was fabricated according to literature (Tong et al., 2016) and made some improvements. The specific preparation process of SCN-CN was as follows: melamine (1.01 g, 0.8 mmol) and a certain amount trithiocyanuric acid (1.41 g, 0.8 mmol) were dissolved in 80 mL ethanol solution (50 %). The solution was then stirred and self-assembled at room temperature for 4 h. Then, the mixture was transferred to an autoclave and heated at 100 ˚C for 6 h. Next, the product was filtered and dried to obtain tubular mixture SCN precursor. After that, 1.21 g of SCN precursor was added to 40 mL ethanol solution and stirred, and then 40 mL ethanol solution was added to the above solution containing a certain amount of urea (0.6 g, 0.9 g, 1.2 g) and stirred for 4 h. The obtained yellow mixtures were filtered, water washed, dried to remove unattached urea, and then calcined at 550 ˚C (2.3 ˚C min^{-1}) under N_2 atmosphere for 4 h in a tube furnace. After the above samples were calcined and ground, they were recorded as SCN-CN-1, SCN-CN-2, and SCN-CN-3, respectively. For comparison, SCN_x with different S doping amounts was prepared without adding urea, where x was the molar ratio of thiocyanuric acid/melamine, namely, $SCN_{0.5}$, SCN_1, $SCN_{1.5}$, and the SCN-CN composite materials in this manuscript correspond to SCN_1. As shown in Fig. S1, different preparation conditions, including dry cure, self-assembly time, pressure, temperature, and solution were investigated for the effect of SCN-CN morphology. In addition, bulk

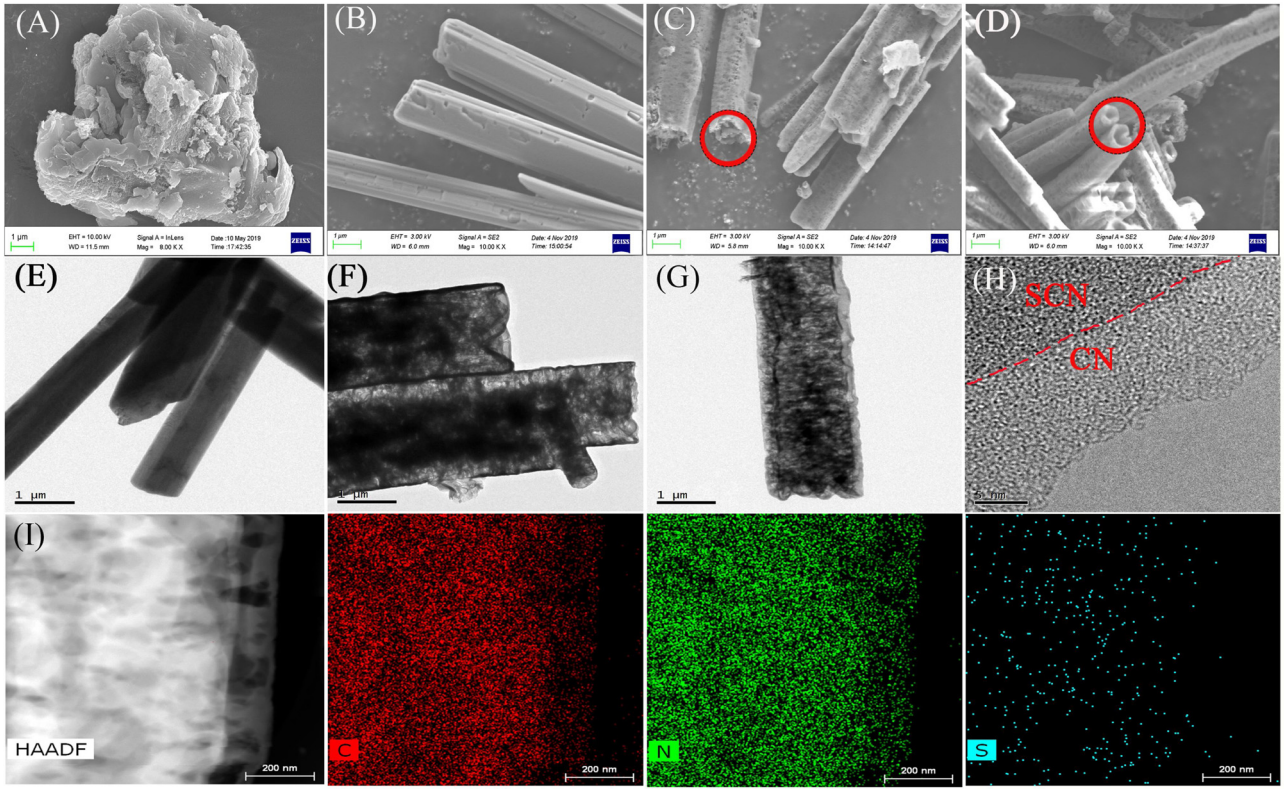

Fig. 1. SEM images of CN (A), SCN precursor (B), SCN (C), and SCN-CN-2 (D); TEM images of SCN precursor (E), SCN (F) and SCN-CN-2 (G); HRTEM images of SCN-CN-2 (I); HAADF-TEM image and EDS mapping images of SCN-CN-2 (I).

carbon nitride CN was obtained by calcining melamine.

2.3. Structural characterization methods

The morphology and microstructure of the samples were revealed by SEM (FEI Quanta-F250, Germany), TEM and HRTEM (FEI Tecnai-G2 F20, Germany). The crystal phase of the samples was obtained using a XRD (Bruker AXS D8, Germany) with a Cu-Ka radiation ($\lambda = 1.5406$ Å). The surface elemental composition was surveyed by XPS (PHI 5300 ESEA, Japan) using the C 1s peak at 284.8 eV as a standard. The specific surface area and pore distribution were measured at -196 °C using an analyzer (Quantachrome Quadrasorb SI, United States). The ultraviolet-visible diffuse reflectance spectra of the samples were obtained with UV–vis diffuse reflectance spectrophotometer ((Shimadzu UV-2600, Japan) using $BaSO_4$ as the standard. The photo-luminescence (PL) spectra performed on a fluorescence spectrometer (Hitachi F-7000, Japan) at the excitation wavelength of 350 nm. The electrochemical impedance spectroscopy (EIS) and photocurrent of the samples were tested on an electrochemical analyzer (CHI 660C, China) in a three-electrode system under VSL illumination. The electron spin resonance (ESR) signals were monitored on a X-band Elexsys system spectrometer (Bruker, Germany). The concentration of total organic carbon (TOC) was examined by an analyzer (Shimadzu TOC-VCPH, Japan). The Zeta potential under different pH values was detected with Zeta-sizer NanoZS (Malvern). Degradation intermediates were detected by liquid chromatography-tandem mass spectrometry (LC-MS) equipped with a G6460 triple quadrupole mass spectrometer and an Agilent 1290 series HPLC (Agilent Technologies, USA).

2.4. Photoreaction apparatus and procedure

To evaluate the photocatalytic behaviors of the SCN-CN, the photocatalytic degradation of 10 mg L^{-1} TCH solution and 20 mg L^{-1} RHB was conducted. In detail, 50 mg sample was added to 50 mL of TCH solution, and 10 mg sample was added to 100 mL of RHB solution. Before irradiation, the suspension was stirred for 30 min in a dark environment to achieve adsorption equilibrium. Then, photocatalytic experiments were carried out under the visible-light irradiation (a 300 W Xe lamp was used as the light source, $\lambda > 420$ nm). The peripheral device of the light source had an ultraviolet filter, which absorbed ultraviolet rays and allows only visible light to pass through. In order to ensure that the incident light intensity was consistent, the distance between the liquid surface of the reaction solution and the light source was fixed at approximately 10 cm in all degradation experiments. And the average visible light intensity was ca. 100 mW cm^{-2} measured by a light meter (HS1010). The total energy consumption of a photocatalytic degradation TCH experiment was about 8.38 KJ (the detailed calculation process was shown in the supporting information). During the TCH irradiation, 1.0 mL suspension was withdrawn every 5 min and analyzed by UV–vis spectrophotometer at the absorption peak of 273 nm. As for RHB, 1.0 mL suspension was withdrawn every 15 min and analyzed by UV–vis spectrophotometer at the absorption peak of 554 nm.

2.5. Theoretical calculation method

The density functional theory (DFT) calculations of samples were carried out with the Vienna ab-initio simulation package (VASP) (Zhu et al., 2019). The geometry optimization calculations were constructed based on Perdew − Burke − Ernzerhof (PBE) in the generalized gradient approximation (GGA). Due to the well-known defects of the GGA-PBE function, the electronic structure and band structure of the model were simulated using HSE06 hybrid function. The cut-off energy was set 340 eV for the plane-wave expansion. The k-point mesh of $6 \times 6 \times 2$ was used to the geometry optimization. A 10 Å vacuum space was introduced to avoid the interference interaction between the neighboring systems. The convergence tolerance parameters for the max step size was 0.001 Å, the maximum force was 0.03 eV/Å, energy change was

1.0×10^{-5} eV/atom and maximum stress was 0.005 GPa.

3. Results and discussion

3.1. Structure and performance analysis of samples

3.1.1. Morphology, crystal and chemical states analysis

Generally, the morphology of the photocatalyst affects the photocatalytic performance. The SCN-CN-2 prepared by different synthetic methods was shown in Fig. S1 and Fig. 1D-E. Compared with Fig. 1D-E, several samples in Fig. S1 had disadvantages such as unstable skeleton structure, easy collapse or breakage, and uneven size. This was mainly because the presence of ethanol in the reaction solution increases the solubility of melamine and trithiocyanuric acid, so that they had better dispersibility and more contact opportunities, resulting in better self-assembly in sufficient time. In addition, under solvothermal conditions, ethanol could be intercalated between carbon nitride layers, which facilitated the stripping of carbon nitride and thus promotes the formation of hollow tubes (Xiao et al., 2019). At the same time, the SCN precursor obtained under autoclave environment had a strong skeleton structure and could maintain the tubular frame structure after compounding by comparing Fig. S1B and Fig. 1D.

The synthesis process of SCN-CN-2 as shown in Scheme 1. In detail, firstly, melamine and trithiocyanuric acid self-assembled through hydrogen bonding and π-π interaction to build supramolecular intermediates, forming a regular one-dimensional structure. Secondly, a thin layer of urea molecule was wrapped on the surface of the SCN precursor by intermolecular forces. Thirdly, the hydrogen bonding interaction between the molecules became weaker in the process of thermal polymerization, leading to the weakening of the supramolecular intermediate and the formation of a hollow structure (Xu et al., 2020). As shown in Fig. 1A-I, the morphological structure of as-prepared samples was characterized by SEM, TEM and HRTEM. The CN (Fig. 1A) exhibited a typical multi-layered block structure, and the SCN precursor (Fig. 1B and F) obtained by drying after self-assembly melamine and trithiocyanuric acid was a solid hexahedral structure with 1 μm in diameter. After SCN precursor calcination, the surface of the obtained SCN became rough, and the hollow structure was partially present. Hollow structure provided more channels for rapid transmission of photo-generated electrons, which facilitated the separation of electrons and holes (Tong et al., 2016; Xu et al., 2020). As for SCN-CN-2, the intermolecular force changes due to the presence of urea on the surface of the SCN precursor, and the surface was covered with a layer of CN by observing Fig. 1F, G (TEM) and Fig. 1H (HRTEM), which confirmed the SCN-CN-2 isotype heterojunction composite was successfully prepared. In addition, the elemental composition and distribution of SCN-CN-2 composites were studied by element mapping spectrometry. The result of element mapping showed the presence and uniform distribution of the C, N and S elements in the SCN-CN-2 composite. It is worth noting that the difference in the distribution of S elements can be observed from the mapping diagram of S. The sporadic S element in CN may be caused by the noise of the test, which can be proved by the S mapping diagram in Fig S1M.

The X-ray diffraction (XRD) pattern of the prepared sample was shown in Fig. 2A. Two main peaks were observed in the XRD pattern of the three samples. The peak at 13.2° indexed to the (100) plane corresponded to the in-plane structure packing pattern of the three-hole-triazine unit in the nitride pore. The other peak around 27.4° corresponded to the interlaminar stacking of the CN aromatic unit, which was indexed to the (002) plane (Deng et al., 2018a). Comparing the intensities of the three peaks, the peak intensity of the SCN was lower, which may be attributed to the fact that the S doping destroys the crystalline region of the CN, resulting in a decrease in the degree of crystallization. Moreover, the weak (100) plane peaks of SCN and SCN-CN-2 indicated a decrease in intermolecular hydrogen bonding interactions after thermal polymerization, and this was also the reason for the formation of hollow structures (Xu et al., 2020).

The pore structure and specific surface area of CN, SCN and SCN-CN-2 were studied by N_2 adsorption-desorption, and the results were shown in Fig. 2B. The N_2 adsorption-desorption isotherms of the three samples belonged to the typical type III isotherm, indicating that all samples had mesoporous structure. At the same time, the pore size distribution of the sample indicated that the pore size was mainly concentrated at about 25 nm, indicating the sample was mainly mesopores.

The specific surface area of the sample (obtained according to the BET method), the pore volume and the average pore diameter (obtained according to the BJH adsorption method) were shown in Table 1. Obviously, SCN-CN-2 has larger pore volume and specific surface area due to the obvious hollow structure, and smaller pore size than that of CN and SCN, which indicates SCN-CN-2 had a rich pore structure and a high specific surface area for the existence of a rich hollow structure. This was closely related to the loose structure of SCN-CN-2 in SEM. Therefore, the SCN-CN-2 complex had more active sites and promotd the adsorption of pollutants on its surface. The increase in adsorption performance was generally considered to promote the contact between the photocatalyst and the pollutants, which is conducive to the progress of photocatalysis (Shao et al., 2019c).

Further investigation of the surface chemical state of the sample was continued using XPS spectroscopy, and the results were shown in Fig. 2C-F. The results in Fig. S2 indicate the presence of C, N and a small amount of O in all samples. It was worth noting that the peak of S is hardly visible, which indicates that the doping level of S in SCN-CN-2 was low, but the obvious S element could be found in the S mapping spectrum. There were two peaks in the high resolution C 1s spectrum (Fig. 2C), which were 287.9 eV assigned to N−CN= in the heterocyclic ring and 284.8 eV to the C−C of the graphite species (Deng et al., 2017). Similarly, there were four peaks, namely 404.2 eV (π excitation), 401.1 eV (C−NH−), 399.9 eV (N–$(C)_3$) and 398.5 eV (C−NC=) in the high-resolution N 1s spectrum (Fig. 2D), respectively. In order to confirm the chemical state of the S element in the sample, XPS was used to test the S 2p in the sample. The presence of a trace amount of S element could be observed in the high-resolution S 2p spectrum (Fig. 2E), and the binding energy of the corresponding peak is 163.9 eV, which indicated that S in the sample exists as a S−C bond by substituting lattice N (Liu et al., 2010). Besides, the valence band of the sample was tested by XPS. According to Fig. 2F, it can be seen that the sample CN hada VB of 2.11 eV and the SCN had a VB of 1.93 eV, which indicated that the doping of S changes the band gap structure of CN. The VB of carbon nitride prepared after S doping was reduced, which was consistent with previous reports in the literature (Wang et al., 2018). Considering the theoretical VB of CN is 1.54 eV, and the VB of SCN was 1.36 eV after adjusted.

The previous XPS results show that S has replaced N atoms in CN and has a low doping density. However, the lower doping ratio requires the larger model structure, which increases the computational costs. Hence, this study used a small theoretical model for approximate replacement as shown in Table 2. Moreover, the possible doping positions are studied and the results were shown in Fig. S3. According to the results of ultraviolet diffuse reflection and previous literature, the SCN band energy value was applicable only when the doping position was SCN_1. After simulation calculation, the optimized geometries of the CN, SCN and SCN-CN-2 composites were shown in Fig. 3.

3.1.2. Optical characteristics and electronic structure analysis

In order to further study the physicochemical properties of as-prepared samples, the photoelectric properties of the samples were analyzed by UV–vis DRS, electrochemical test and PL. From the UV–vis DRS spectrum of Fig. 4A, it was apparent that all of the samples exhibited significant absorption of ultraviolet light ($\lambda < 420$ nm). The SCN and SCN-CN-2 prepared by doping S had stronger absorption ability for VSL ($\lambda > 420$ nm) than the original CN, which was

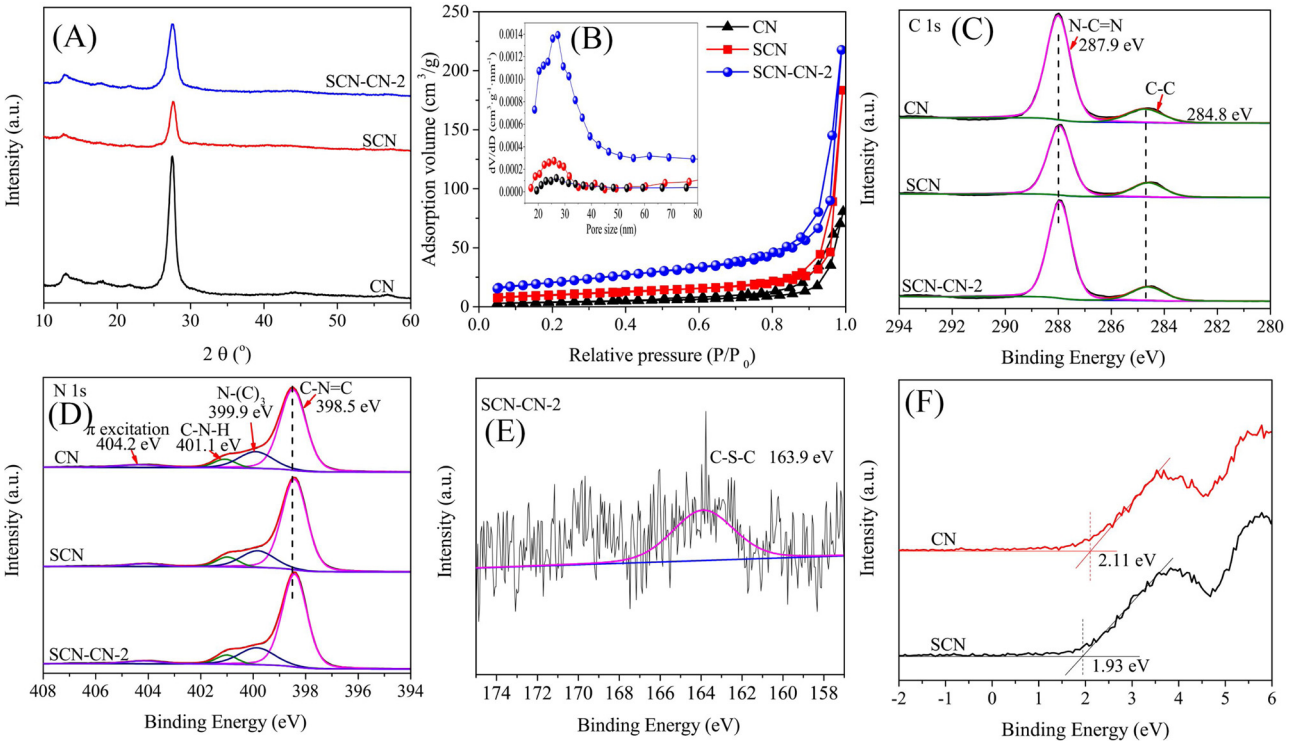

Fig. 2. XRD patterns of as-prepared samples (A); N_2 adsorption and desorption isotherms and pore size distributions of as-prepared samples (B); XPS spectra of as-prepared samples: C 1s spectrum (C), N 1s spectrum (D), S 2p spectrum (E), and valence band (F).

Table 1
The pore structure parameters of CN, SCN, and SCN-CN-2.

Sample	BET surface area (m^2/g)	Pore volume (cm^3/g)	Average pore size (nm)
CN	23.33	0.25	31.86
SCN	35.24	0.28	32.66
SCN-CN-2	73.45	0.34	18.30

Table 2
Lattice parameters of the samples.

Samples	Lattice types	Lengths (Å)			Angles (°)		
		a	b	c	α	β	γ
CN	3D triclinic	7.13	7.13	14.08	90	90	120
SCN	3D triclinic	7.13	7.13	14.08	90	90	120
SCN-CN-2	3D triclinic	7.13	7.13	14.08	90	90	120

consistent with the results simulated using theoretical calculations (Fig. 4B). Generally, strong absorption ability ws beneficial to enhance the photogenerated electron efficiency and improve the photocatalytic degradation efficiency. Consequently, the SCN-CN-2 isotype heterojunction had a high photo-generated carrier capacity and fast photocatalytic efficiency under VSL. The E_g of the sample was calculated according to the Eq. (1) (Shao et al., 2018), and the E_g of CN SCN and SCN-CN-2 were 2.72 eV, 2.66 eV and 2.92 eV (Fig. 4C), respectively, which was consistent with the literature report (Wang et al., 2018).

$$\alpha h\nu = A(h\nu - E_g)^{n/2} \quad (1)$$

Where α, h, ν and A represent the absorption coefficient, Planck constant, optical frequency and constant, respectively. The value of n depends on the type of semiconductor, and n is equal to 4 for CN.

In order to further analyze the band structure, the band structures of samples were calculated by the HSE06 functional and were shown in Fig. 4D-F. From them, we concluded that the E_g of CN, SCN and SCN-CN-2 were 2.70 eV, 2.82 eV and 2.92 eV, respectively, which is consistent with the results reported in previous literature and shows the rationality of our theoretical calculation model (Liu et al., 2010). The E_g of samples obtained by theoretical calculation were very close to the experimental values except for SCN. This might be caused by the difference in structure of the SCN. The theoretically calculated value was the single-layer SCN, and the experimental value corresponded to the tubular SCN. The results of the theoretical settlement also demonstrated that the band gap structure of the composite material was affected and improved, which was consistent with the UV–vis spectrum and XPS spectra. Additionally, the valence band and conduction band position of the sample could also be obtained from the band structure diagram. The valence band top (VBT) and the conduction band bottom (CBB) of CN and SCN were both located at points G and F, respectively, which indicated that CN and SCN were both indirect bandgap semiconductor (Shao et al., 2019c).

To further study the interface of the SCN-CN-2 isotype heterojunction, the partial density of states (PDOS) of samples calculated and analyzed, and Fig. 5 showed the total density of states (TDOS) and PDOS of samples. It is well known that the denser of curve in the band diagram, the higher peak in the corresponding DOS diagram and the more electrons, which means that the generation of carriers is facilitated in the photocatalytic process. Obviously, the energy band structure of SCN-CN-2 composites was tighter than that of others, which might be due to the formation of isotype heterojunctions. As a result, SCN-CN-2 had better photocatalytic properties than that of others.

Furthermore, we revealed the orbital state of the electrons in the sample through TDOS and PDOS, and the results were shown in Fig. 5. In the CN (Fig. 5A), VBT was mainly contributed by C 2s, 2p and N 2s, 2p orbital hybridization, while CBB was mainly derived from C 2p and N 2p orbital hybridization. As for SCN (Fig. 5B), VBT was mainly contributed by C 2s, 2p, N 2s, 2p and S 3s, 3p orbitals, while CBB was mainly composed of C 2p, N 2p and S 3p. Because the S 3p orbital energy was higher than the orbital energy of C 2p, it would cause the

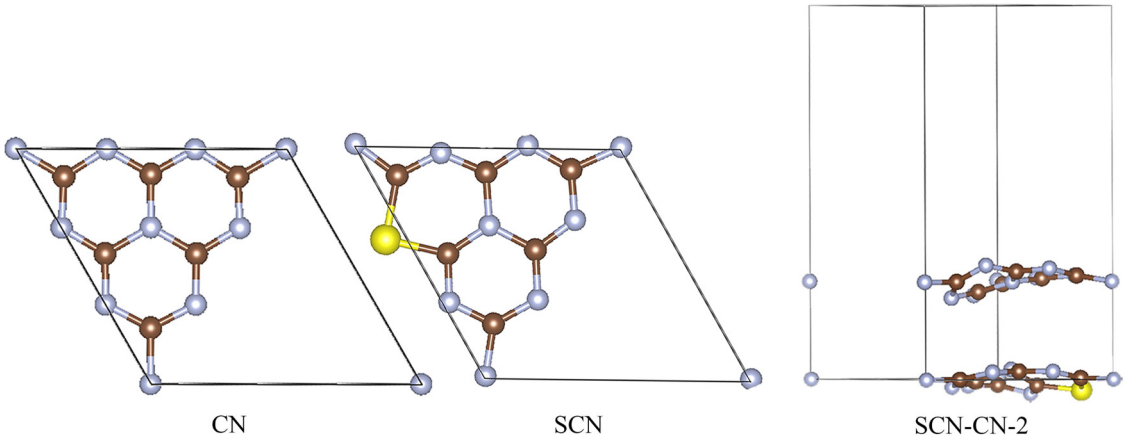

Fig. 3. The optimized geometric structures of CN, SCN and SCN-CN-2, and the brown, gray and yellow represent C, N and S atoms, respectively.

VBT of SCN to upshift, which was consistent with the XPS valence band (Ma et al., 2018). As for the SCN-CN-2 complex (Fig. 5C), VBT was occupied by C 2s, 2p, N 2s, 2p and S 3s, 3p orbitals, while CBB was mainly composed of C and N atoms. Thence, combination the results of band structures and DOS results, we could infer that the E_g of SCN-CN-2 increased on account of the orbital hybridization between the CN and SCN. It was worth noting that the DOS at the Fermi level of SCN-CN-2 composites was significantly higher than that of SCN and CN, which indicated that SCN-CN-2 has high carrier mobility (Li et al., 2019; Kou et al., 2019).

3.1.3. Photoelectrochemical performance analysis

Photoelectrochemical performance is considered to be valid evidence for evaluating photocurrent response and photogenerated electron separation of photocatalysts. As shown in Fig. 6A, the SCN-CN-2 composite exhibited higher transient photocurrent intensity under VSL illumination than that of CN and SCN, indicating that the SCN-CN-2 composite had better photogenerated e^--h^+ pairs separation efficiency. This was most likely attribute the presence of defects, ordered tubulars, and isotype heterojunction structures formed between CN and SCN. In addition, electrochemical impedance EIS is an important indicator to measure carrier mobility. As shown in Fig. 6B, the SCN-CN-2 composite had smaller arc than that of CN and SCN, indicating that the SCN-CN-2 composite had the lower carrier migration resistance. In short, the above characterization results indicated that the structure of the tubular SCN-CN-2 isotype heterojunction has high separation and transfer efficiency of photogenerated carriers, thereby improving its photocatalytic performance (Yuan et al., 2019).

In order to further investigate the separation and transfer efficiency of photogenerated carriers, the PL was analyzed. As shown in Fig. 6C, all samples illustrated significant emission peaks near 475 nm owing recombination of the e^--h^+ pairs. Importantly, the SCN-CN-2 composite had the lower PL emission intensity compared with other samples, indicating that the SCN-CN-2 composite had the higher photo-generated e^--h^+ pairs separation efficiency and excellent photocatalytic performance. The synergy in lattice defects, the ordered tubular structure and the isotype heterojunction interface played a crucial role in promoting the separation of photogenerated carriers and prolonging

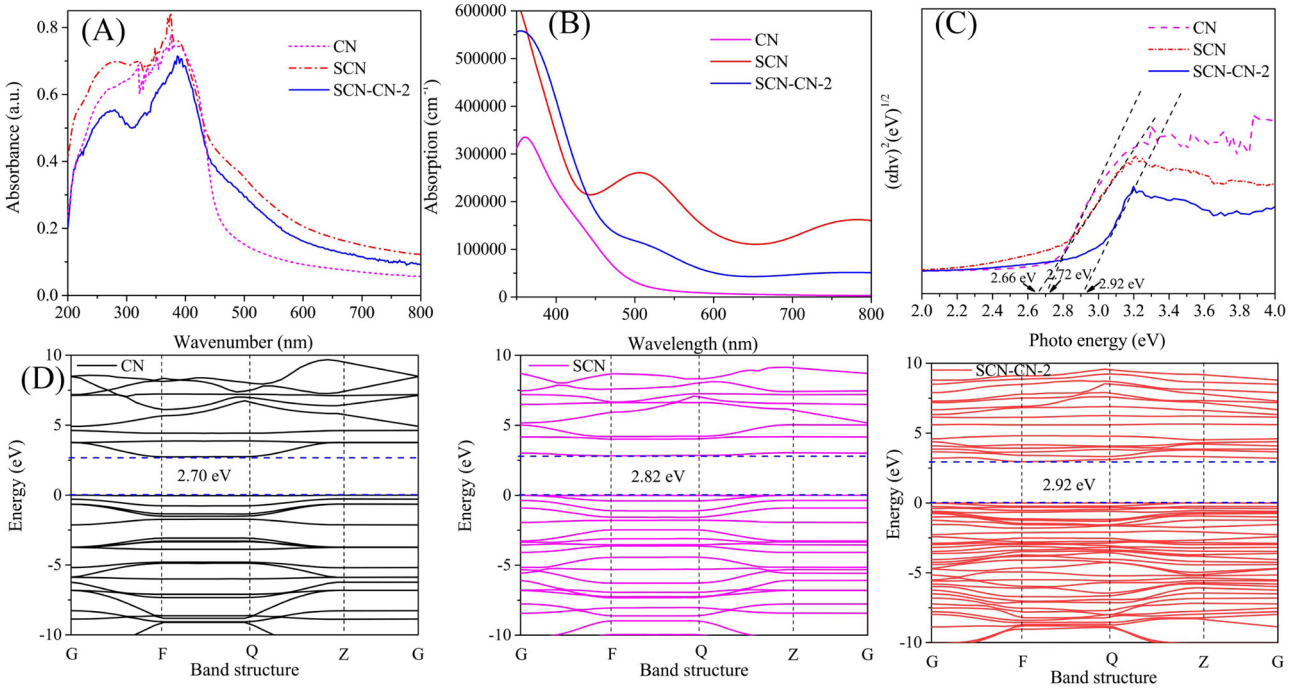

Fig. 4. UV–vis DRS spectrum of as-prepared samples (A); The absorption spectra of CN, SCN and SCN-CN-2 obtained by theoretical calculations (B); The band gap energies of CN, SCN and SCN-CN-2 (C); The band structures of CN, SCN and SCN-CN-2 (D).

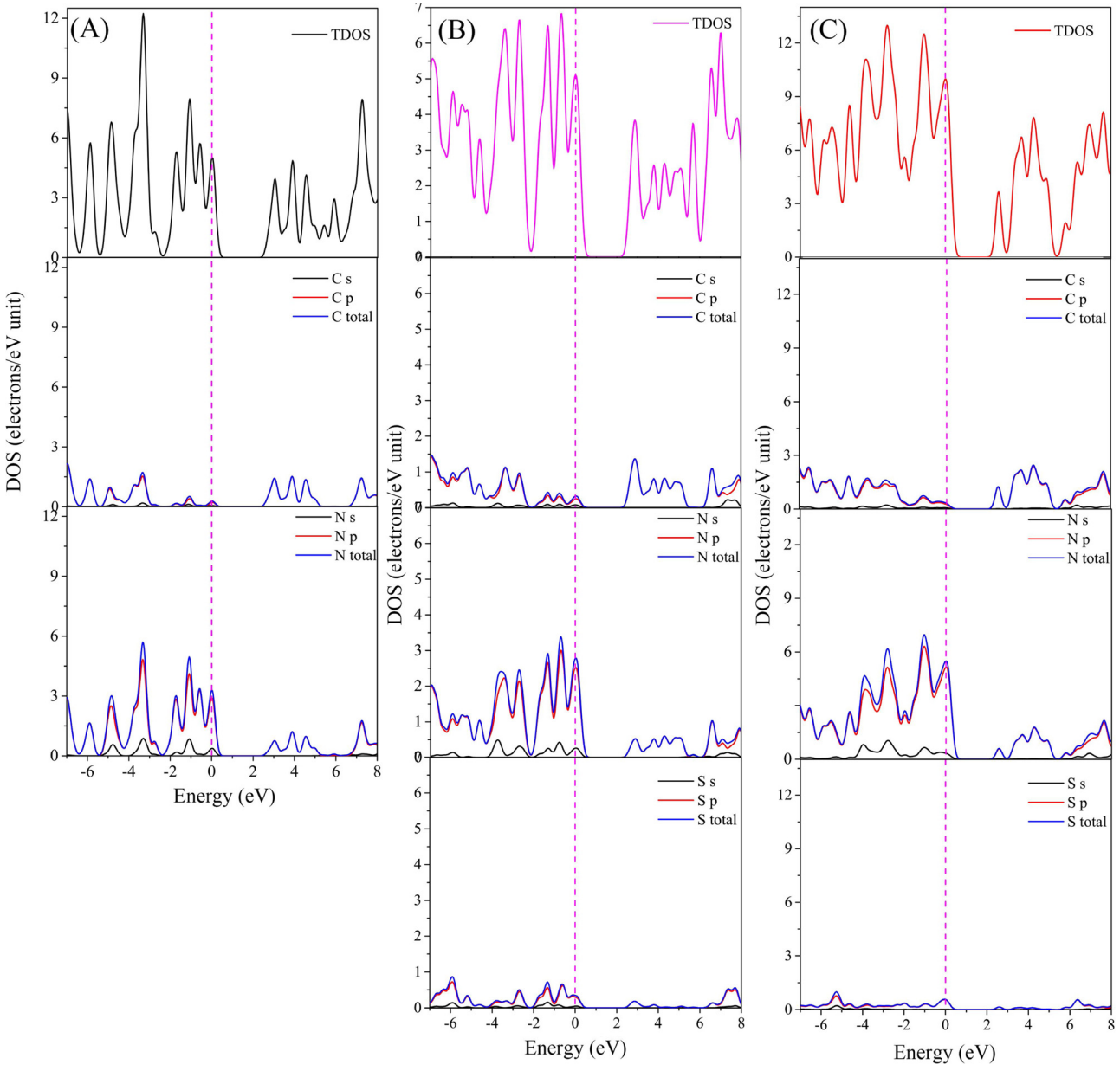

Fig. 5. The TDOS and PDOS of CN (A), SCN (B) and SCN-CN-2 (C).

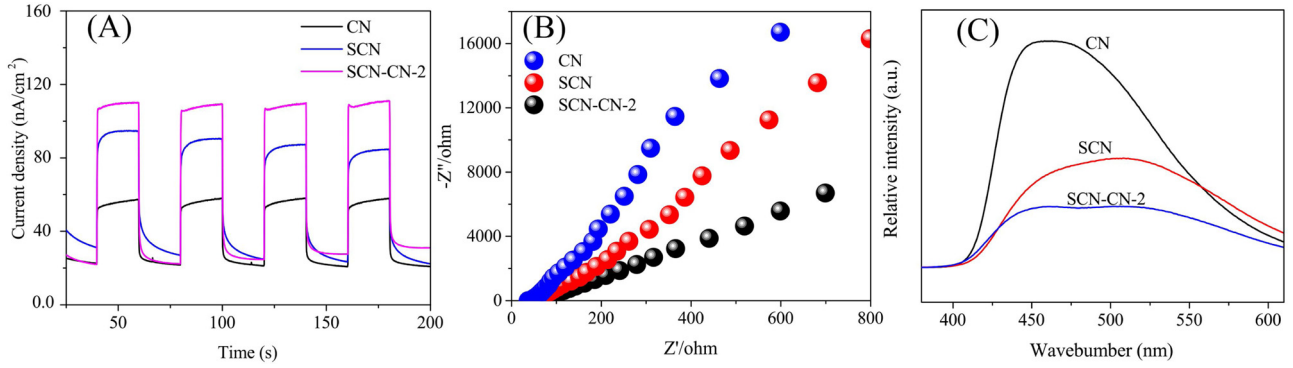

Fig. 6. The photocurrent (A), EIS (B), and PL (C) of as-prepared samples.

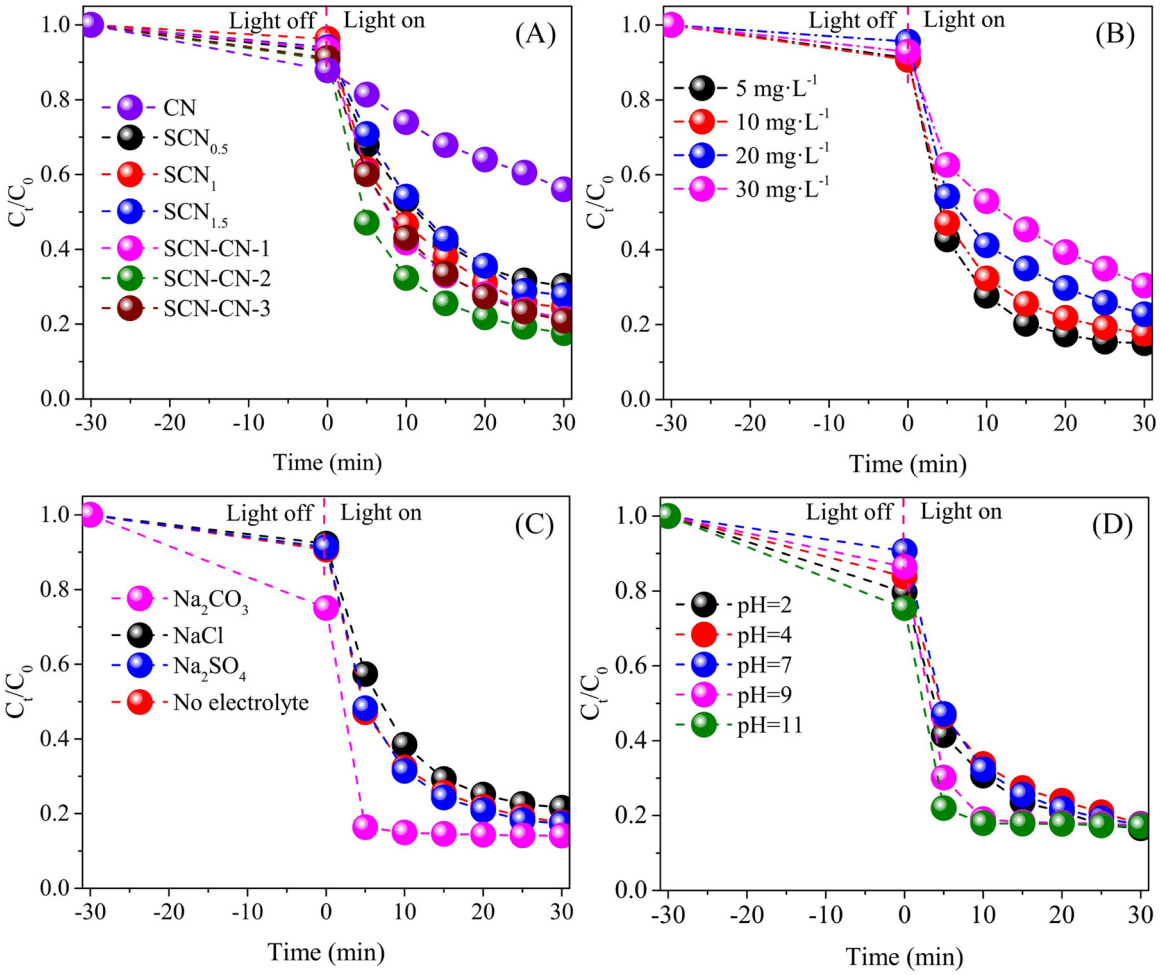

Fig. 7. The photocatalytic activities of as-prepared samples for TCH degradation under visible light (λ > 420 nm) (A); The Effect of initial concentration (B), supporting electrolytes (C), and solution pH (D) for TCH degradation by SCN-CN-2 under visible light.

the lifetime of carriers (Tong et al., 2016; Wu et al., 2018).

3.2. Photocatalytic properties

3.2.1. Photodegradation of TCH and RHB

The photocatalytic properties of the as-prepared photocatalysts were assessed through photo-degradation of TCH under VSL irradiation. The as-prepared photocatalysts exhibited a low adsorption capacity for TCH (Fig. 7A). The SCN-CN isotype heterojunction had a significantly higher photocatalytic activity than that of CN and SCN, and they were in the order of SCN-CN-2 > SCN-CN-3 > SCN-CN-1 > SCN_1 > $SCN_{1.5}$ > $SCN_{0.5}$ > CN. Compared with the original CN, the photocatalytic efficiency of SCN obtained by S-doping was obviously improved, which might be credited to the doping of S improving the band gap structure, enhancing the absorption of VSL and forming a regular tubular structure according to the previous conclusion. It was worth emphasizing that the photocatalyst SCN-CN-2 prepared after two-step modification had a rapid degradation efficiency for TCH (82.6 % within 30 min), which was significantly faster than that of CN (44.0 %) and SCN (75.5 %). The increase in photocatalytic efficiency of these composites might be as a result of the presence of isotype heterojunctions between SCN and CN, which facilitated the transmission of electrons and the separation of e^--h^+. In short, the synergy between the components improved VSL absorption, accelerated the separation of e^--h^+, and optimized surface and structure, which could be confirmed by UV–vis spectrum, PL and N_2 adsorption-desorption isotherms, respectively. In addition, in order to deepen the understanding of the TCH degradation behavior of the sample, the experimental results were fitted by the pseudo-first-order kinetic model and pseudo-second-order kinetic model, and the results were shown in Fig. S5A. Compared with the result obtained by fitting the pseudo-first-order kinetic model, the degradation process of TCH by SCN-CN-2 was more consistent with the pseudo-second-order kinetic model. In order to test the universal applicability of the catalyst, we also studied its photocatalytic degradation of the common organic dye RHB. The results were shown in Fig. S4A. SCN-CN-2 (96.2 % within 60 min) showed a significantly improved ability to degrade RHB under visible light compared to CN (4.8 %) and SCN_1 (53.2 %). Next, a systematic degradation study of currently popular antibiotic contaminant TCH was performed in this paper. In addition, we detected the production of trace amounts of H_2O_2 measured by iodometry in the process of SCN-CN degradation of TCH (Fig. S4B), which was conducive to the production of ·OH and improve photocatalytic performance (Yang et al., 2019a).

3.2.2. Effects of initial antibiotic concentrations

In actual wastewater, the initial concentration of contaminants is variable. Therefore, it is important to study the photocatalytic degradation properties of photocatalysts at different contaminant concentrations. The degradation performance of SCN-CN-2 against TCH at different initial concentrations (5 − 30 mg L^{-1}) was shown in Fig. 7B. As the concentration of pollutants decreases, the degradation efficiency of TCH by SCN-CN-2 increased. With the increase of initial TCH concentration, the photocatalytic efficiencies of SCN-CN-2 to TCH were

84.95 %, 82.40 %, 77.24 %, and 69.55 %, respectively. The results of photocatalytic degradation of different contaminant concentrations indicated that the high initial contaminant concentrations are detrimental to photocatalytic removal of contaminants. This is because the increase in the concentration of pollutants leads to a decrease in the photon transmission path and light transmittance, and further reduces the phenomenon of photons migrating to the active part of the photocatalyst. In addition, intermediates produced during photocatalytic degradation compete with TCH molecules for limited reaction sites (Deng et al., 2018b). Although the initial concentration of high contaminants would inhibit the photocatalytic rate of SCN-CN-2 composite to a certain extent, SCN-CN-2 had the higher removal rate of antibiotics at low concentrations (5 mg L^{-1}). Considering the concentration of pollutants in actual wastewater was low, SCN-CN-2 was conducive to application in practical wastewater.

3.2.3. Effect of supporting electrolytes

In the actual water environment, some anions, such as chlorine, sulfate and bicarbonate ions, often coexist in the water environment. Therefore, the influences of NaCl, Na_2SO_4 and Na_2CO_3 (0.05 M) were studied for the photocatalytic degradation of TCH by SCN-CN-2. As shown in Fig. 7C, the addition of Cl^- and the addition SO_4^{2-} had almost no effect on photocatalytic degradation. However, the addition of CO_3^{2-} can significantly improve the adsorption of TCH by SCN-CN-2 and the photocatalytic degradation efficiency. This was due to the hydrolysis of CO_3^{2-} to form HCO_3^- and OH^-, which led to the formation of alkaline solutions (pH ~ 11). Combined with the effect of pH on TCH in Fig. 7D, SCN-CN-2 adsorption TCH was facilitated under alkaline conditions. Therefore, the addition of CO_3^{2-} significantly increased the removal efficiency of photocatalytic degradation of TCH.

3.2.4. Effects of reaction pH

The reaction pH is another important factor affecting photocatalytic degradation in actual wastewater and the generation of ROSs. In this study, gradients of pH (2.04, 3.89, 6.85, 9.05, 11.09) were adjusted by NaOH (0.1 M) or HNO_3 (0.1 M). The Zeta potentials of SCN-CN-2 changed from positive to negative as pH increases (Table 3). The results showed that the negative charge of CN, SCN and SCN-CN-2 gradually decreases, which was consistent with the results reported in the literature (Liu et al., 2018d). This might be due to the change in electronic properties of carbon nitride due to S doping. The presence of a lone pair of electrons N delocalizes the remaining lone electrons into the p-conjugated triazine ring, which results in an electron-rich state, so it has the most negative charges (Zhang et al., 2019b). After S replaces N, the lone pair of electrons in the system decreased, resulting in a decrease in the negative charge value. At the same time, the hydrophobicity and static electricity of the material could be clearly observed during the experiment, which might be related to the reduction of oxygen-containing functional groups in the material. The reduction of oxygen-containing groups means that the negative value of the ZETA potential of the material decreases (He et al., 2018).

As shown in Fig. 7D, SCN-CN-2 had no significant effect on the degradation of TCH under acidic conditions. Nevertheless, the adsorption amount and photocatalytic degradation efficiency of SCN-CN-2 on TCH increased significantly under alkaline conditions, which was due to the increased electrostatic interaction between SCN-CN-2 and TCH (Deng et al., 2018c). The increase in the amount of adsorption led to easier contact between antibiotics and the surface of the photocatalyst, which was beneficial to improve photocatalytic degradation efficiency. Meanwhile, according to the degradation pathway of TCH in Fig. 11, the degradation process of TCH might be affected under alkaline conditions, such as promoting the demethylation of TCH (Zhang et al., 2014). Therefore, SCN-CN-2 showed a rapid photocatalytic degradation to TCH of 78 % in 5 min under alkaline environment. In short, the SCN-CN-2 photocatalyst exhibited good stability for photocatalytic degradation of TCH in a wide pH range, which was conducive to resisting complex environments in practical applications. It was worth emphasizing that SCN-CN-2 showed rapid photocatalytic degradation efficiency at the initial stage under alkaline conditions.

Table 3
The Zeta potentials of samples prepared in different pH solution.

pH		2.04	3.89	6.85	9.05	11.09
Zeta potential	SCN-CN-2	24.6	15.5	−11.4	−28.8	−55.0
	SCN	23.1	15.1	−13.6	−47.5	−55.9
	CN	18.9	9.72	−24.8	−49.8	−52.4

3.2.5. Mineralization capacity and photostability tests

The mineralization capacity and reusability are two very important indicators in the practical application of photocatalyst. The mineralization ability of the antibiotics by the CN, SCN and SCN-CN-2 complexes was tested by TOC. The TOC in the original TCH solution was set to 100 %, and the results of TOC_t measured at different times were shown in Fig. 8A. The SCN-CN-2 composite exhibited good mineralization ability, and the mineralization efficiency of TCH is 79 % under 3 h' illumination. Compared with SCN-CN-2, the mineralization efficiency of CN and SCN samples for TCH was only 31 % and 58 %, respectively.

The SCN-CN-2 composite was tested for reusability under VSL illumination. After each degradation cycle, the photocatalyst was regenerated by filtration, ethanol washing and drying, and then used in the next cycle. As shown in Fig. 8B, the photodegradation efficiency of SCN-CN-2 for TCH only reduced by 2.51 % after five cycles, which may be due to the close isotype heterojunction between the composite catalysts by bonding or π-π interaction. At the same time, there is almost no change in the XRD pattern before and after the use of SCN-CN-2 (Fig. 8C), which indicates that the photocatalyst has a relatively stable structure. All in all, the above results indicate that the SCN-CN-2 isotype heterojunction composite has good mineralization ability and reusability, resulting in great application potential in practical applications.

3.3. Photocatalytic mechanism

3.3.1. Active substances during degradation

In order to reveal the photocatalytic degradation mechanism of SCN-CN-2 composites on TCH, the main active substances ($\cdot O_2^-$, ·OH, h^+) in the photocatalysis process were studied firstly. Three common scavengers (1 mmol), 4-hydroxy-TEMPO (HTEMPO, $\cdot O_2^-$ scavenger), isopropanol (IPA, ·OH scavenger) and disodium edetate (EDTA-2Na, h^+ scavenger) were used, and the results were shown in Fig. 9A. In the presence of any scavenger, it would affect the degradation efficiency of TCH, indicating the photocatalytic degradation process was related to all three active substances. Compared with other scavengers, the photodegradation efficiency of TCH decreased most in the presence of scavenger EDTA-2Na, indicating h^+ play a major role in the photocatalytic process. Similarly, the addition of HTEMPO also had a large negative impact on the degradation of TCH, indicating that $\cdot O_2^-$ also played an important role in the degradation of TCH. In short, the process of degrading TCH at SCN-CN-2 by the above results was that h^+, $\cdot O_2^-$ and ·OH are jointly controlled in the photocatalytic process, in which h^+ and $\cdot O_2^-$ played a leading role.

Furthermore, the presence of the active material in the photocatalytic process by ESR characterization continues to be verified, and the results were shown in Fig. 9B and C. DMPO-$\cdot O_2^-$ and DMPO-·OH had no peaks in the dark conditions. However, both DMPO-$\cdot O_2^-$ and DMPO-·OH were able to observe significant characteristic peaks after VSL irradiation, and the intensity of the peaks increased with the increase of the illumination time. Therefore, it was confirmed the presence of the active substances $\cdot O_2^-$ and ·OH in the SCN-CN-2 composite

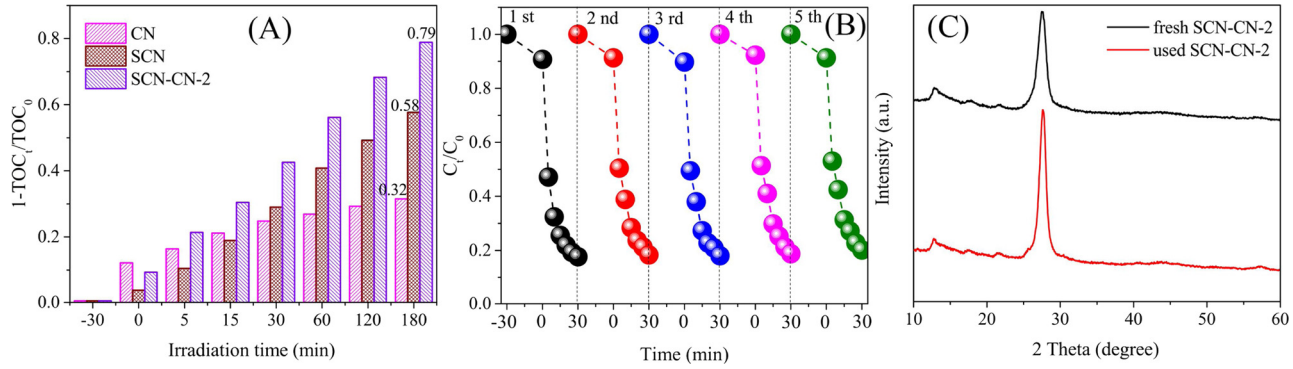

Fig. 8. The TOC removal of TCH by CN, SCN and SCN-CN-2 composite under VSL illumination for 3 h (A); The cyclic experiments of SCN-CN-2 composite for the degradation of TCH (B); The XRD pattern of the SCN-CN-2 composite before and after 5 cycle photocatalytic experiments (C).

photocatalytic system. Through free radical quenching experiments and ESR characterization, it was proved that h^+, $\cdot O_2^-$ and ·OH played a synergistic role during the photocatalytic degradation of TCH by SCN-CN-2 composites.

3.3.2. Charge transfer

In order to study the charge transfer at the interface of SCN-CN-2 composite, the work function of the sample was simulated by GGA-PBE function. The work function was calculated by calculation combined with the following Eq. (2) (Wang et al., 2019a):

$$\Phi = E_{vacuum} - E_F \quad (2)$$

Among them, E_{vacuum} and E_F represent the energy of the electrostatic potential in vacuum and the Fermi level in the vacuum near the surface, respectively, where that of vacuum is set as 0.

As shown in Fig. 10A, the work functions of CN, SCN and SCN-CN-2 were 4.82, 3.67 and 4.22 eV, respectively. The low work function indicated that the photocatalyst is prone to photogenerated electrons, resulting in S-doped SCN had higher photocatalytic activity than CN (Miao et al., 2018). Meanwhile, because the Fermi energy of SCN was higher than that of CN, causing electrons transfer from the SCN to the CN when they were in contact until the Fermi level tends to be uniform (Sun et al., 2014). It was worth emphasizing that understanding the work function and the magnitude relationship of the Fermi level was critical to the electron transport mechanism of the composite photocatalyst, which is unfortunately often ignored.

In addition, the band gap structure of the semiconductor is important for determining the direction of electron transfer in the composite photocatalyst and revealing the photocatalytic mechanism. The valence band, conduction band and E_g of CN and SCN obtained by XPS and the UV–vis DRS spectrum. The mechanism of charge separation at the interface in the SCN-CN-2 isotype heterojunction structure under VSL illumination was proposed in Fig. 10B. For CN, E_g was 2.72 eV, E_{VB} was 1.54 eV, and E_{CB} was -1.18 eV. Similarly, as for SCN, the E_g, E_{VB}, and E_{CB} are 2.66, 1.36, and -1.30 eV, respectively. Because the work function and Fermi level in Fig. 10A show that SCN had a lower work function and a higher Fermi level than that of CN, causing internal electrons to move from the SCN to the CN until the Fermi level was equal when they were contact (Chen et al., 2018). Accompanying the energy band bending during the balancing process, the energy band of the CN would move downward, and the energy band of the SCN moves upward, which was consistent with the calculation of the charge differential density. Therefore, photo-generated electrons in the CB of the CN rapidly migrated at the CB of the SCN due to a good match of band structure overlap and tight interfacial interactions. The specific transmission process was as follows: both CN and SCN can generate electrons and holes in CB and VB under VSL irradiation, respectively. The electrons at the CB in the CN migrate to the CB of the SCN, conversely, the holes in the VB of the SCN are transferred to the VB of the CN. In this way, photogenerated electrons and holes could be effectively separated. In addition, the one-dimensional structure could also control the charge carriers to transport in the longitudinal direction, resulting in the effective separation of electrons and holes, thereby promoting photocatalysis.

To verify the direction of electron transfer of SCN-CN-2 interface, the charge difference density of SCN-CN-2 was calculated, and the results were shown in Fig. 10C. The green area indicated a decrease in charge and the red area indicates charge accumulation. Comparing the charge distribution map and the charge cut-off diagram of SCN-CN-2, charge redistribution occurred primarily in the SCN-CN-2 interface region. A region with significant electron increase was observed from Fig. 10C, mainly due to structural deformation caused by π-π interaction between CN and SCN. In order to analyze the charge transfer at the interface intuitively, we performed a 2D slice of the charge difference density. It could be seen that the electrons at the CN decrease, while the

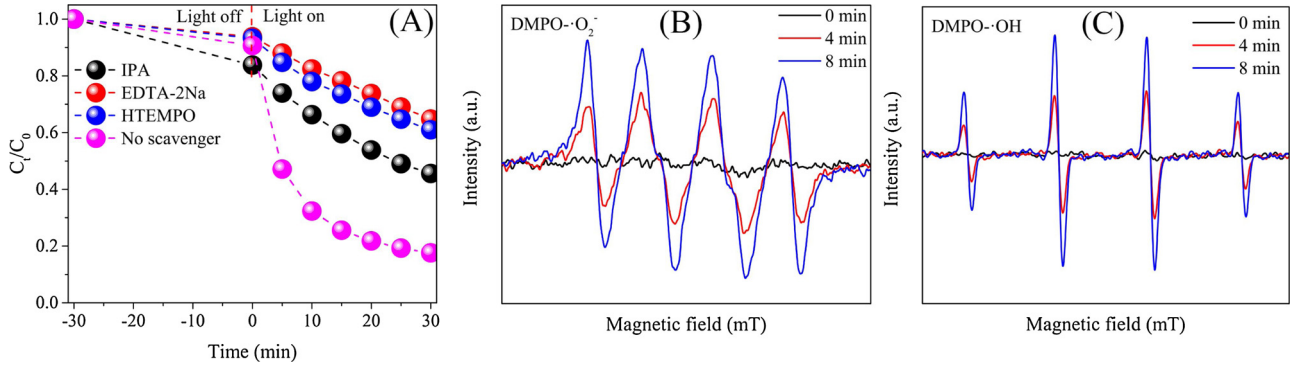

Fig. 9. The trapping experiment of radical species during the photocatalytic degradation of TCH by SCN-CN-2 composite under visible light illumination (A); The ESR spectra of radical adducts trapped by DMPO- $\cdot O_2^-$ (B) and ·OH (C) in SCN-CN-2 dispersion in the dark and under visible light illumination.

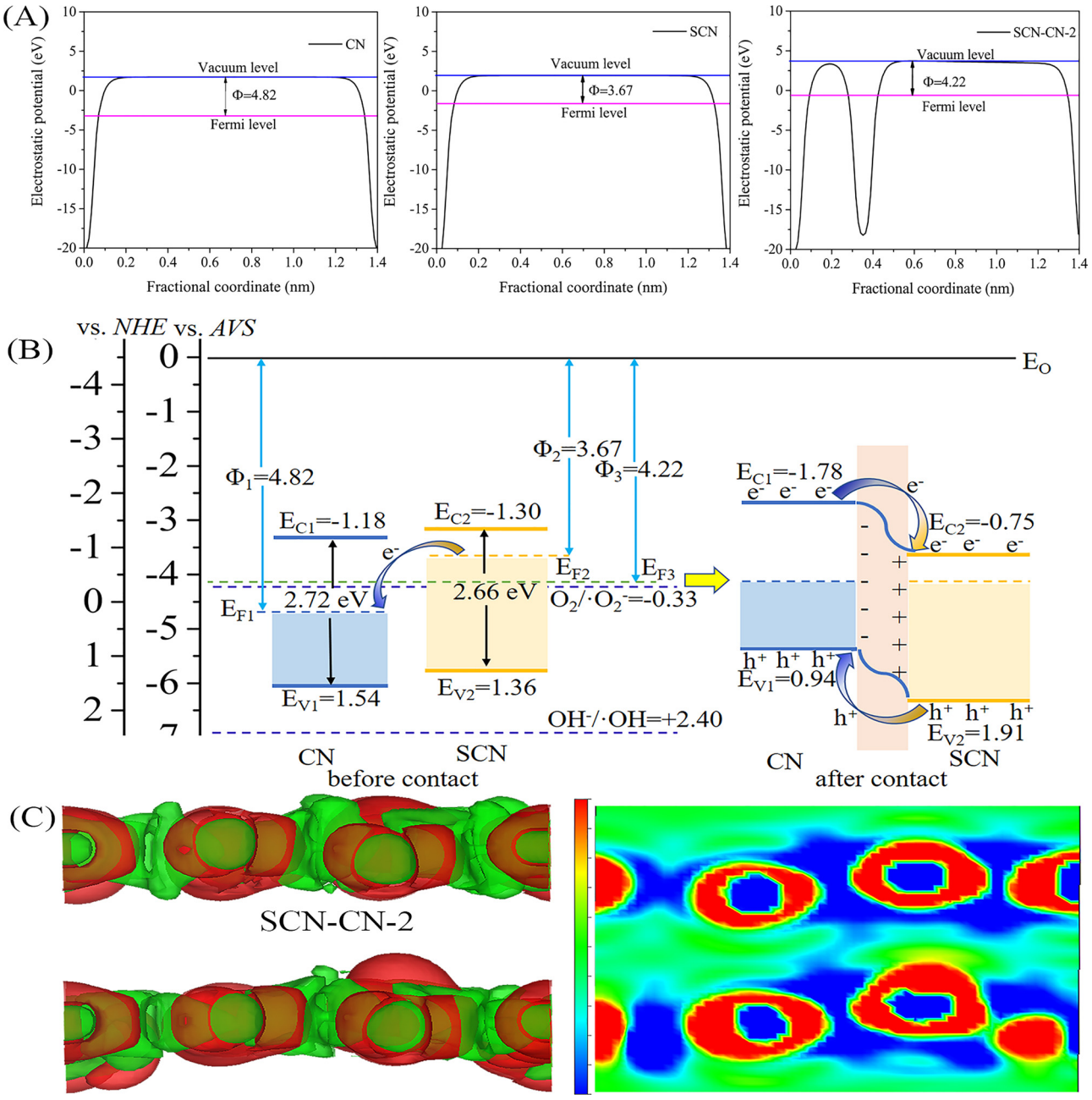

Fig. 10. The work function of CN, SCN and SCN-CN-2, and the pink and blue lines represent the Fermi level and the vacuum level, respectively (A); The proposed mechanism of band structure and charge separation at the interface in the SCN-CN-2 isotype heterojunction structure under visible light illumination, and the relationship between NHE and AVS is $E_{NHE} = -E_{AVS} - 4.5$ (Zhu et al., 2018) (B); The charge difference density of SCN-CN-2, red and green refer to electron-rich and electron-deficient areas, respectively (C).

electrons at the SCN increased. That was, the electron-rich region appeared on the surface of the SCN, and a hole-rich region appeared on the surface of the CN, which caused the formation of an internal electric field. This electron transport process played a key role in the construction of the electric field inside the heterojunction system. The internal electric field could significantly enhance the ability of photoelectrons to transfer from the CN to the SCN and inhibit the recombination of the e^--h^+ pair. Therefore, the calculation of the differential charge shows that the electrons were transferred from CN to SCN, which was consistent with the derivation.

According to the relationship between the conduction band and valence band of each semiconductor in SCN-CN-2, we could draw the following conclusions. The conduction band edge potential of CN and SCN was larger than the potential of $O_2/\cdot O_2^-$ (-0.33 eV), resulting in the electrons on CB of CN could participate in the reduction process of O_2 to $\cdot O_2^-$. However, because the valence edge potentials of CN and SCN were more negative than the potentials of $OH^-/\cdot OH$ (2.40 eV) and $H_2O/\cdot OH$ (2.72 eV), it was not possible to directly generate ·OH. The holes and $\cdot O_2^-$ might be directly involved in the oxidation reaction of TCH, which was consistent with the experimental results of the scavengers (Tong et al., 2016). On the one hand, according to the band-gap structure relationship, electrons and holes could be efficiently transferred and molecules were at the SCN-CN-2 interface. On the other hand, it was worth noting that the ordered tubular structure of SCN-CN-2 played an important role in separation of electrons and holes and improve photocatalytic performance (Yang et al., 2019b). Therefore, due to the presence of the tubular structure, electrons and holes could be transferred in the opposite longitudinal direction, which facilitated

efficient separation of electrons and holes. In addition, the adsorption-desorption results of N_2 indicate that SCN-CN-2 had a high specific surface area and a rich porosity, which resulted in the photocatalyst having many active sites for adsorbing contaminants, thereby contributing to the improvement of photocatalytic performance. In summary, due to the synergy between the SCN-CN-2 isotype heterojunction and the tubular structure, SCN-CN-2 had high photocatalytic properties. The main possible reactions of photocatalytic degradation of TCH by SCN-CN-2 photocatalytic system were as follows:

$$\text{SCN-CN-2} + \text{VSL} \rightarrow \text{SCN-CN-2}(e^-/h^+) \quad (3)$$

$$e^- + O_2 \rightarrow \cdot O_2^- \quad (4)$$

$$\cdot O_2^- + H^+ \rightarrow \cdot OOH \quad (5)$$

$$\cdot OOH + H^+ + e^- \rightarrow H_2O_2 \quad (6)$$

$$H_2O_2 + e^- \rightarrow \cdot OH + OH^- \quad (7)$$

$$h^+ + \cdot O_2^- + \cdot OH + \text{TCH} \rightarrow \text{Degradation products} \quad (8)$$

3.4. Degradation path analysis

In order to study the path of SCN-CN-2 photocatalytic degradation of TCH, some major degradation products in the photodegradation process were detected by LC–MS, and the LC–MS spectra of the TCH intermediates eluted at different reaction time are shown in Fig. S6. There are 11 intermediates, named P1 ~ P11. The same or similar intermediates have been reported, and the possible information of the intermediates are shown in Table S1. Next, based on the structure of these intermediates, three possible degradation pathways were proposed as shown in Fig. 11.

For pathway A, it mainly includeed dealkylation, deamination and dehydration processes. The N-demethylation process produced a TCH intermediate P_1 (*m/z* 431) due to the low C—N bond energy (Cao et al., 2018a). Then, P_1 formed an intermediate P_2 (*m/z* 384) by losing the N-methyl group, the methyl group and the two hydroxyl groups. Next, P_2 formed the intermediate product P_3 (*m/z* 339) by deamination. Subsequently, P_3 continued to decompose with the with the reaction proceeds. For pathway B, it mainly included the addition reaction of carbon-carbon double bond and dehydration reaction (Mboula et al., 2012). The carbon-carbon double bond in aromatic ring of TCH was attacked by ·OH to form an intermediate P_4 (*m/z* 461) firstly. Next, ·OH was continuously attacked P_4 to obtain the intermediate product P_5 (*m/z* 477). Then, a dehydration reaction occurred in P_5 to obtain P_6 (*m/z* 459). Similarly, P_6 continued to be photocatalyzed by degradation with the reaction proceeds. For pathway C, it mainly included dealkylation and dehydration processes (Cao et al., 2018b). The TCH was subjected to a dehydration reaction to form P_7 (*m/z* 427) firstly, and then an N-methyl group removal reaction occurred due to a low energy of the C—N bond to form P_8 (*m/z* 400). Then, the acylamino group in P_8 was attacked by the living radical to form the P_9 (*m/z* 362). At the same time, due to the presence of strong oxidizing ·OH and $\cdot O_2^-$, the carbocyclic ring in P_8 could be directly cleaved to form P_{10} (*m/z* 318). Next, P_{10} could be further oxidized to the intermediate P_{11} (*m/z* 274). Similarly, as the photocatalytic reaction proceeds, P_{11} continued to be degraded into small molecules.

4. Conclusions

In this paper, we had successfully synthesized tubular SCN-CN-2 isotype heterojunction by molecular self-assembly and thermal polymerization methods. The SCN-CN-2 isotype heterojunction had good morphology, strong VSL absorption capacity, high specific surface area and porosity, fast electron transport rate and good separation efficiency of photogenerated electrons and holes by several characterization techniques. Meanwhile, the tubular structure enabled efficient separation of electron-hole pairs in the longitudinal direction. Therefore, SCN-CN-2 composite exhibited a rapid degradation for TCH (82.6 % within 30 min) and RHB (96.2 % within 60 min), which was significantly faster than that of CN and SCN. Furthermore, the energy band structure, density of state, optical properties, work function, charge differential density and degradation path of photocatalyst were studied by DFT theoretical calculation. Moreover, the SCN-CN-2 was effective to handle complex wastewater, including different contaminant concentrations, pH and supporting electrolytes, and the photodegradation efficiency of SCN-CN-2 on TCH was significantly improved under alkaline environment. According to the results of LC-MS, the possible degradation paths of TCH were proposed. Mechanism analysis demonstrated that the active substances h^+ and $\cdot O_2^-$ played a leading role in the photodegradation system. This research may provide new insights for the construction of new and efficient photocatalysts and promote their practical application in environmental remediation. Besides, this research also provides a combination of theory and calculation methods to reveal the properties of photocatalysts and degradation mechanisms.

CRediT authorship contribution statement

Qinghua Liang: Conceptualization, Writing - original draft, Data

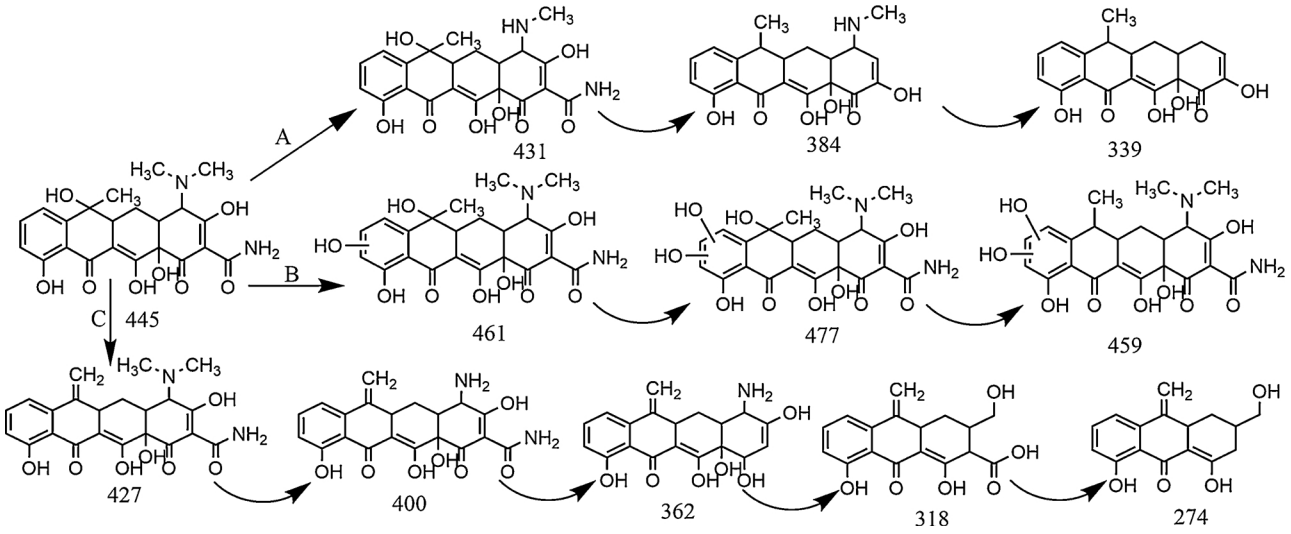

Fig. 11. The proposed photocatalytic degradation pathway of TCH and the chemical structure of intermediates.

curation, Investigation, Methodology. **Xiaojuan Liu:** Writing - review & editing, Validation. **Jiajia Wang:** Writing - review & editing, Validation. **Yang Liu:** Writing - review & editing. **Zhifeng Liu:** Funding acquisition, Resources, Supervision, Project administration. **Lin Tang:** Funding acquisition, Resources, Supervision, Project administration. **Binbin Shao:** Formal analysis, Software, Visualization. **Wei Zhang:** Writing - review & editing. **Shanxi Gong:** Software, Visualization. **Min Cheng:** Writing - review & editing. **Qingyun He:** Writing - review & editing. **Chengyang Feng:** Formal analysis.

Declaration of Competing Interest

The authors declare that they have no known competing financial interests or personal relationships that could have appeared to influence the work reported in this paper.

Acknowledgments

The study was financially supported by the Program for Changjiang Scholars and Innovative Research Team in University (IRT-13R17), the National Natural Science Foundation of China (51979103, 51679085, 51579096, 51521006, 51508177), the Fundamental Research Funds for the Central Universities of China (531107050930, 531107051205), the Funds of Hunan Science and Technology Innovation Project (2018RS3115), the Key Research and Development Project of Hunan Province of China (2017SK2241). The authors also gratefully acknowledge the National Supercomputing Center in Changsha for providing the computing resources.

Appendix A. Supplementary data

Supplementary material related to this article can be found, in the online version, at doi:https://doi.org/10.1016/j.jhazmat.2020.123355.

References

Cao, J., Xiong, Z., Lai, B., 2018a. Effect of initial pH on the tetracycline (TC) removal by zero-valent iron: adsorption, oxidation and reduction. Chem. Eng. J. 343, 492–499.
Cao, J., Yang, Z.-h., Xiong, W.-p., Zhou, Y.-y., Peng, Y.-r., Li, X., Zhou, C.-y., Xu, R., Zhang, Y.-r., 2018b. One-step synthesis of Co-doped UiO-66 nanoparticle with enhanced removal efficiency of tetracycline: simultaneous adsorption and photocatalysis. Chem. Eng. J. 353, 126–137.
Chen, Y., Shi, T., Liu, P., Ma, X., Shui, L., Shang, C., Chen, Z., Wang, X., Kempa, K., Zhou, G., 2018. Insights into the mechanism of the enhanced visible-light photocatalytic activity of black phosphorus/BiVO4 heterostructure: a first-principles study. J. Mater. Chem. A 6, 19167–19175.
Chen, X., Shi, R., Chen, Q., Zhang, Z., Jiang, W., Zhu, Y., Zhang, T., 2019. Three-dimensional porous g-C3N4 for highly efficient photocatalytic overall water splitting. Nano Energy 59, 644–650.
Deng, Y., Tang, L., Zeng, G., Zhu, Z., Yan, M., Zhou, Y., Wang, J., Liu, Y., Wang, J., 2017. Insight into highly efficient simultaneous photocatalytic removal of Cr(VI) and 2,4-diclorophenol under visible light irradiation by phosphorus doped porous ultrathin g-C 3 N 4 nanosheets from aqueous media: performance and reaction mechanism. Appl. Catal. B, Environ. 203, 343–354.
Deng, Y., Tang, L., Feng, C., Zeng, G., Chen, Z., Wang, J., Feng, H., Peng, B., Liu, Y., Zhou, Y., 2018a. Insight into the dual-channel charge-charrier transfer path for nonmetal plasmonic tungsten oxide based composites with boosted photocatalytic activity under full-spectrum light. Appl. Catal. B Environ. 235, 225–237.
Deng, Y., Tang, L., Zeng, G., Wang, J., Zhou, Y., Wang, J., Tang, J., Wang, L., Feng, C., 2018b. Facile fabrication of mediator-free Z-scheme photocatalyst of phosphorous-doped ultrathin graphitic carbon nitride nanosheets and bismuth vanadate composites with enhanced tetracycline degradation under visible light. J. Colloid Interface Sci. 509, 219–234.
Deng, Y., Tang, L., Feng, C., Zeng, G., Wang, J., Zhou, Y., Liu, Y., Peng, B., Feng, H., 2018c. Construction of plasmonic Ag modified phosphorous-doped ultrathin g-C3N4 nanosheets/BiVO4 photocatalyst with enhanced visible-near-infrared response ability for ciprofloxacin degradation. J. Hazard. Mater. 344, 758–769.
Dong, F., Zhao, Z., Xiong, T., Ni, Z., Zhang, W., Sun, Y., Ho, W.-K., 2013. In situ construction of g-C3N4/g-C3N4 metal-free heterojunction for enhanced visible-light photocatalysis. ACS Appl. Mater. Interfaces 5, 11392–11401.
Feng, C., Deng, Y., Tang, L., Zeng, G., Wang, J., Yu, J., Liu, Y., Peng, B., Feng, H., Wang, J., 2018. Core-shell Ag2CrO4/N-GQDs@g-C3N4 composites with anti-photocorrosion performance for enhanced full-spectrum-light photocatalytic activities. Appl. Catal. B, Environ. 239, 525–536.
Guo, S., Deng, Z., Li, M., Jiang, B., Tian, C., Pan, Q., Fu, H., 2016. Phosphorus-doped carbon nitride tubes with a layered micro-nanostructure for enhanced visible-light photocatalytic hydrogen evolution. Angew. Chem. Int. Ed. 55, 1830–1834.
He, P., Tang, X., Chen, L., Xie, P., He, L., Zhou, H., Zhang, D., Fan, T., 2018. Patterned carbon nitride-based hybrid aerogel membranes via 3D printing for broadband solar wastewater remediation. Adv. Funct. Mater. 28.
He, Q., Xu, P., Zhang, C., Zeng, G., Liu, Z., Wang, D., Tang, W., Dong, H., Tan, X., Duan, A., 2019. Influence of surfactants on anaerobic digestion of waste activated sludge: acid and methane production and pollution removal. Crit. Rev. Biotechnol. 39, 746–757.
Jiang, Y., Liu, Z., Zeng, G., Liu, Y., Shao, B., Li, Z., Liu, Y., Zhang, W., He, Q., 2018a. Polyaniline-based adsorbents for removal of hexavalent chromium from aqueous solution: a mini review. Environ. Sci. Pollut. Res. Int. 25, 6158–6174.
Jiang, L., Yuan, X., Zeng, G., Liang, J., Wu, Z., Wang, H., Zhang, J., Xiong, T., Li, H., 2018b. A facile band alignment of polymeric carbon nitride isotype heterojunctions for enhanced photocatalytic tetracycline degradation. Environ.-Sci. Nano 5, 2604–2617.
Kou, Z., Wang, T., Gu, Q., Xiong, M., Zheng, L., Li, X., Pan, Z., Chen, H., Verpoort, F., Cheetham, A.K., Mu, S., Wang, J., 2019. Rational design of holey 2D nonlayered transition metal Carbide/Nitride heterostructure nanosheets for highly efficient water oxidation. Adv. Energy Mater., 1803768.
Li, G., Lian, Z., Wang, W., Zhang, D., Li, H., 2016. Nanotube-confinement induced size-controllable g-C3N4 quantum dots modified single-crystalline TiO2 nanotube arrays for stable synergetic photoelectrocatalysis. Nano Energy 19, 446–454.
Li, W., Rodriguez-Castellon, E., Bandosz, T.J., 2017. Photosensitivity of g-C3N4/S-doped carbon composites: study of surface stability upon exposure to CO2 and/or water in ambient light. J. Mater. Chem. A 5, 24880–24891.
Li, J., Li, Y., Zhang, G., Huang, H., Wu, X., 2019. One-dimensional/two-dimensional core-shell-structured Bi2O4/BiO2- x heterojunction for highly efficient broad spectrum light-driven photocatalysis: faster interfacial charge transfer and enhanced molecular oxygen activation mechanism. ACS Appl. Mater. Interfaces 11, 7112–7122.
Liang, Q., Li, Z., Bai, Y., Huang, Z.-H., Kang, F., Yang, Q.-H., 2017. A composite polymeric carbon nitride with in situ formed isotype heterojunctions for highly improved photocatalysis under visible light. Small 13.
Liang, Q., Liu, X., Zeng, G., Liu, Z., Tang, L., Shao, B., Zeng, Z., Zhang, W., Liu, Y., Cheng, M., Tang, W., Gong, S., 2019. Surfactant-assisted synthesis of photocatalysts: mechanism, synthesis, recent advances and environmental application. Chem. Eng. J. 372, 429–451.
Liu, G., Niu, P., Sun, C., Smith, S.C., Chen, Z., Lu, G.Q., Cheng, H.M., 2010. Unique electronic structure induced high photoreactivity of sulfur-doped graphitic C3N4. J. Am. Chem. Soc. 132, 11642–11648.
Liu, Z., Zeng, Z., Zeng, G., Li, J., Zhong, H., Yuan, X., Liu, Y., Zhang, J., Chen, M., Liu, Y., Xie, G., 2012. Influence of rhamnolipids and Triton X-100 on adsorption of phenol by Penicillium simplicissimum. Bioresour. Technol. 110, 468–473.
Liu, Y., Xiao, H., Goddard, W.A., 2016. 3rd, schottky-barrier-Free contacts with two-dimensional semiconductors by surface-engineered MXenes. J. Am. Chem. Soc. 138, 15853–15856.
Liu, H., Chen, D., Wang, Z., Jing, H., Zhang, R., 2017. Microwave-assisted molten-salt rapid synthesis of isotype triazine-/heptazine based g-C3N4 heterojunctions with highly enhanced photocatalytic hydrogen evolution performance. Appl. Catal. B Environ. 203, 300–313.
Liu, Z., Liu, Y., Zeng, G., Shao, B., Chen, M., Li, Z., Jiang, Y., Liu, Y., Zhang, Y., Zhong, H., 2018a. Application of molecular docking for the degradation of organic pollutants in the environmental remediation: a review. Chemosphere 203, 139–150.
Liu, Z., Shao, B., Zeng, G., Chen, M., Li, Z., Liu, Y., Jiang, Y., Zhong, H., Liu, Y., Yan, M., 2018b. Effects of rhamnolipids on the removal of 2,4,2,4-tetrabrominated biphenyl ether (BDE-47) by Phanerochaete chrysosporium analyzed with a combined approach of experiments and molecular docking. Chemosphere 210, 922–930.
Liu, Y., Liu, Z., Zeng, G., Chen, M., Jiang, Y., Shao, B., Li, Z., Liu, Y., 2018c. Effect of surfactants on the interaction of phenol with laccase: molecular docking and molecular dynamics simulation studies. J. Hazard. Mater. 357, 10–18.
Liu, G., Qiao, X., Gondal, M.A., Liu, Y., Shen, K., Xu, Q., 2018d. Comparative study of pure g-C3N4 and sulfur-doped g-C3N4 catalyst performance in photo-degradation of persistent pollutant under visible light. J. Nanosci. Nanotechnol. 18, 4142–4154.
Liu, Y., Cheng, M., Liu, Z., Zeng, G., Zhong, H., Chen, M., Zhou, C., Xiong, W., Shao, B., Song, B., 2019a. Heterogeneous Fenton-like catalyst for treatment of rhamnolipid-solubilized hexadecane wastewater. Chemosphere 236, 124387.
Liu, Y., Liu, Z., Huang, D., Cheng, M., Zeng, G., Lai, C., Zhang, C., Zhou, C., Wang, W., Jiang, D., 2019b. Metal or metal-containing nanoparticle@ MOF nanocomposites as a promising type of photocatalyst. Coord. Chem. Rev. 388, 63–78.
Liu, Q., Shen, J., Yu, X., Yang, X., Liu, W., Yang, J., Tang, H., Xu, H., Li, H., Li, Y., Xu, J., 2019c. Unveiling the origin of boosted photocatalytic hydrogen evolution in simultaneously (S, P, O)-Codoped and exfoliated ultrathin g-C3N4 nanosheets. Appl. Catal. B, Environ. 248, 84–94.
Luo, W., Chen, X., Wei, Z., Liu, D., Yao, W., Zhu, Y., 2019. Three-dimensional network structure assembled by g-C3N4 nanorods for improving visible-light photocatalytic performance. Appl. Catal. B, Environ. 255, 117761.
Ma, Z., Li, Y., Lv, Y., Sa, R., Li, Q., Wu, K., 2018. Synergistic effect of doping and compositing on photocatalytic efficiency: a case study of La2Ti2O7. ACS Appl. Mater. Interfaces 10, 39327–39335.
Mahzoon, S., Nowee, S.M., Haghighi, M., 2018. Synergetic combination of 1D-2D g-C3N4 heterojunction nanophotocatalyst for hydrogen production via water splitting under visible light irradiation. Renew. Energy 127, 433–443.
Mboula, V.M., Hequet, V., Gru, Y., Colin, R., Andres, Y., 2012. Assessment of the efficiency of photocatalysis on tetracycline biodegradation. J. Hazard. Mater. 209, 355–364.

Miao, X., Yue, X., Ji, Z., Shen, X., Zhou, H., Liu, M., Xu, K., Zhu, J., Zhu, G., Kong, L., Shah, S.A., 2018. Nitrogen-doped carbon dots decorated on g-C3N4/Ag3PO4 photocatalyst with improved visible light photocatalytic activity and mechanism insight. Appl. Catal. B Environ. 227, 459–469.

Pan, Y., Liu, X., Zhang, W., Liu, Z., Zeng, G., Shao, B., Liang, Q., He, Q., Yuan, X., Huang, D., Chen, M., 2020. Advances in photocatalysis based on fullerene C60 and its derivatives: properties, mechanism, synthesis, and applications. Appl. Catal. B Environ. 265, 118579.

Romanos, G.E., Athanasekou, C.P., Katsaros, F.K., Kanellopoulos, N.K., Dionysiou, D.D., Likodimos, V., Falaras, P., 2020. Double-side active TiO2-modified nanofiltration membranes in continuous flow photocatalytic reactors for effective water purification. J. Hazard. Mater. 211-212, 304–316.

Ruan, Q., Luo, W., Xie, J., Wang, Y., Liu, X., Bai, Z., Carmalt, C.J., Tang, J., 2017. A nanojunction polymer photoelectrode for efficient charge transport and separation. Angew. Chem. Int. Ed. 56, 8221–8225.

Shao, B., Liu, Z., Zeng, G., Wu, Z., Liu, Y., Cheng, M., Chen, M., Liu, Y., Zhang, W., Feng, H., 2018. Nitrogen-doped hollow mesoporous carbon spheres modified g-C3N4/Bi2O3 direct dual semiconductor photocatalytic system with enhanced antibiotics degradation under visible light. ACS Sustain. Chem. Eng. 6, 16424–16436.

Shao, B., Liu, Z., Zeng, G., Liu, Y., Yang, X., Zhou, C., Chen, M., Liu, Y., Jiang, Y., Yan, M., 2019a. Immobilization of laccase on hollow mesoporous carbon nanospheres: noteworthy immobilization, excellent stability and efficacious for antibiotic contaminants removal. J. Hazard. Mater. 362, 318–326.

Shao, B., Liu, X., Liu, Z., Zeng, G., Liang, Q., Liang, C., Cheng, Y., Zhang, W., Liu, Y., Gong, S., 2019b. A novel double Z-scheme photocatalyst Ag3PO4/Bi2S3/Bi2O3 with enhanced visible-light photocatalytic performance for antibiotic degradation. Chem. Eng. J. 368, 730–745.

Shao, B., Liu, X., Liu, Z., Zeng, G., Zhang, W., Liang, Q., Liu, Y., He, Q., Yuan, X., Wang, D., Luo, S., Gong, S., 2019c. Synthesis and characterization of 2D/0D g-C3N4/CdS-nitrogen doped hollow carbon spheres (NHCs) composites with enhanced visible light photodegradation activity for antibiotic. Chem. Eng. J.

Shao, B., Wang, J., Liu, Z., Zeng, G., Tang, L., Liang, Q., He, Q., Wu, T., Liu, Y., Yuan, X., 2020. Ti3C2Tx MXene decorated black phosphorus nanosheets with improved visible-light photocatalytic activity: experimental and theoretical studies. J. Mater. Chem. A 8, 5171–5185.

Sun, L., Qi, Y., Jia, C.-J., Jin, Z., Fan, W., 2014. Enhanced visible-light photocatalytic activity of g-C3N4/Zn2GeO4 heterojunctions with effective interfaces based on band match. Nanoscale 6, 2649–2659.

Sun, H., Jiang, Z., Wu, D., Ye, L., Wang, T., Wang, B., An, T., Wong, P.K., 2019a. Defect-type-Dependent near-infrared-Driven photocatalytic bacterial inactivation by defective Bi2 S3 nanorods. ChemSusChem 12, 890–897.

Sun, Y., Zhou, Z., Huang, Z., Wu, J., Zhou, L., Cheng, Y., Liu, J., Zhu, C., Yu, M., Yu, P., Zhu, W., Liu, Y., Zhou, J., Liu, B., Xie, H., Cao, Y., Li, H., Wang, X., Liu, K., Wang, X., Wang, J., Wang, L., Huang, W., 2019b. Band structure engineering of interfacial semiconductors based on atomically thin lead iodide crystals. Adv. Mater., e1806562.

Tang, L., Feng, C., Deng, Y., Zeng, G., Wang, J., Liu, Y., Feng, H., Wang, J., 2018. Enhanced photocatalytic activity of ternary Ag/g-C 3 N 4 /NaTaO 3 photocatalysts under wide spectrum light radiation: the high potential band protection mechanism. Appl. Catal. B Environ. 230, 102–114.

Tong, Z., Yang, D., Sun, Y., Nan, Y., Jiang, Z., 2016. Tubular g-C3N4 isotype heterojunction: enhanced visible-light photocatalytic activity through cooperative manipulation of oriented electron and hole transfer. Small 12, 4093–4101.

Triantis, T.M., Fotiou, T., Kaloudis, T., Kontos, A.G., Falaras, P., Dionysiou, D.D., Pelaez, M., Hiskia, A., 2020. Photocatalytic degradation and mineralization of microcystin-LR under UV-A, solar and visible light using nanostructured nitrogen doped TiO2. J. Hazard. Mater. 211-212, 196–202.

Wang, J., Tang, L., Zeng, G., Deng, Y., Liu, Y., Wang, L., Zhou, Y., Guo, Z., Wang, J., Zhang, C., 2017. Atomic scale g-C 3 N 4 /Bi 2 WO 6 2D/2D heterojunction with enhanced photocatalytic degradation of ibuprofen under visible light irradiation. Appl. Catal. B Environ. 209, 285–294.

Wang, H., Bian, Y., Hu, J., Dai, L., 2018. Highly crystalline sulfur-doped carbon nitride as photocatalyst for efficient visible-light hydrogen generation. Appl. Catal. B Environ. 238, 592–598.

Wang, X.D., Huang, Y.H., Liao, J.F., Jiang, Y., Zhou, L., Zhang, X.Y., Chen, H.Y., Kuang, D.B., 2019a. In situ construction of a Cs2SnI6 perovskite Nanocrystal/SnS2 nanosheet heterojunction with boosted interfacial charge transfer. J. Am. Chem. Soc. 141, 13434–13441.

Wang, W., Fang, J., Chen, H., Bao, N., Lu, C., 2019b. Rice-husk-derived mesoporous 0D/2D C3N4 isotype heterojunction with improved quantum effect for photodegradation of tetracycline antibiotics. Ceram. Int. 45, 2234–2240.

Wu, Z., Yuan, X., Zeng, G., Jiang, L., Zhong, H., Xie, Y., Wang, H., Chen, X., Wang, H., 2018. Highly efficient photocatalytic activity and mechanism of Yb3+/Tm3+ co-doped In2S3 from ultraviolet to near infrared light towards chromium (VI) reduction and rhodamine B oxydative degradation. Appl. Catal. B Environ. 225, 8–21.

Wu, T., Liu, X., Liu, Y., Cheng, M., Liu, Z., Zeng, G., Shao, B., Liang, Q., Zhang, W., He, Q., Zhang, W., 2020. Application of QD-MOF composites for photocatalysis: energy production and environmental remediation. Coord. Chem. Rev. 403, 213097.

Xiao, Y., Tian, G., Li, W., Xie, Y., Jiang, B., Tian, C., Zhao, D., Fu, H., 2019. Molecule self-assembly synthesis of porous few-layer carbon nitride for highly efficient photoredox catalysis. J. Am. Chem. Soc. 141, 2508–2515.

Xu, F., Mo, Z., Yan, J., Fu, J., Song, Y., El-Alamia, W., Wu, X., Li, H., Xu, H., 2020. Nitrogen-rich graphitic carbon nitride nanotubes for photocatalytic hydrogen evolution with simultaneous contaminant degradation. J. Colloid Interface Sci. 560, 555–564.

Yang, X., Qian, F., Zou, G., Li, M., Lu, J., Li, Y., Bao, M., 2016. Facile fabrication of acidified g-C3N4/g-C3N4 hybrids with enhanced photocatalysis performance under visible light irradiation. Appl. Catal. B Environ. 193, 22–35.

Yang, Y., Zeng, Z., Zeng, G., Huang, D., Xiao, R., Zhang, C., Zhou, C., Xiong, W., Wang, W., Cheng, M., Xue, W., Guo, H., Tang, X., He, D., 2019a. Ti3C2 Mxene/porous g-C3N4 interfacial Schottky junction for boosting spatial charge separation in photocatalytic H2O2 production. Appl. Catal. B Environ. 258.

Yang, H., Xu, B., Yuan, S., Zhang, Q., Zhang, M., Ohno, T., 2019b. Synthesis of Y-doped CeO2/PCN nanocomposited photocatalyst with promoted photoredox performance. Appl. Catal. B Environ. 243, 513–521.

Yu, H., Jiang, L., Wang, H., Huang, B., Yuan, X., Huang, J., Zhang, J., Zeng, G., 2019. Modulation of Bi2 MoO6 -based materials for photocatalytic water Splitting and environmental application: a critical review. Small 15, e1901008.

Yuan, Y.-J., Shen, Z., Wu, S., Su, Y., Pei, L., Ji, Z., Ding, M., Bai, W., Chen, Y., Yu, Z.-T., Zou, Z., 2019. Liquid exfoliation of g-C3N4 nanosheets to construct 2D-2D MoS2/g-C3N4 photocatalyst for enhanced photocatalytic H2 production activity. Appl. Catal. B Environ. 246, 120–128.

Zhang, J., Zhang, M., Sun, R.Q., Wang, X., 2012. A facile band alignment of polymeric carbon nitride semiconductors to construct isotype heterojunctions. Angew. Chem. Int. Ed. 51, 10145–10149.

Zhang, X., Yao, J., Li, D., Chen, X., Wang, H., Yeo, L.Y., Friend, J.R., 2014. Self-assembled highly crystalline TiO2 mesostructures for sunlight-driven, pH-responsive photodegradation of dyes. Mater. Res. Bull. 55, 13–18.

Zhang, S., Liu, Y., Gu, P., Ma, R., Wen, T., Zhao, G., Li, L., Ai, Y., Hu, C., Wang, X., 2019a. Enhanced photodegradation of toxic organic pollutants using dual-oxygen-doped porous g-C3N4: mechanism exploration from both experimental and DFT studies. Appl. Catal. B, Environ. 248, 1–10.

Zhang, C., Liu, J., Huang, X., Chen, D., Xu, S., 2019b. Multistage polymerization design for g-C3N4 nanosheets with enhanced photocatalytic activity by modifying the polymerization process of melamine. ACS Omega 4, 17148–17159.

Zhao, D., Chen, Z., Yang, W., Liu, S., Zhang, X., Yu, Y., Cheong, W.C., Zheng, L., Ren, F., Ying, G., Cao, X., Wang, D., Peng, Q., Wang, G., Chen, C., 2019. MXene (Ti3C2) vacancy-confined single-atom catalyst for efficient functionalization of CO2. J. Am. Chem. Soc. 141, 4086–4093.

Zhu, B., Zhang, J., Jiang, C., Cheng, B., Yu, J., 2017. First principle investigation of halogen-doped monolayer g-C3N4 photocatalyst. Appl. Catal. B, Environ. 207, 27–34.

Zhu, B., Zhang, L., Cheng, B., Yu, J., 2018. First-principle calculation study of tri-s-triazine-based g-C3N4: a review. Appl. Catal. B, Environ. 224, 983–999.

Zhu, Z., Tang, X., Wang, T., Fan, W., Liu, Z., Li, C., Huo, P., Yan, Y., 2019. Insight into the effect of co-doped to the photocatalytic performance and electronic structure of g-C3N4 by first principle. Appl. Catal. B Environ. 241, 319–328.